Investigation of gas diffusion electrode systems for the electrochemical CO2 conversion

Investigation of Gas Diffusion Electrode systems for the electrochemical CO_2 conversion

Hilmar Guzmán,[a,b,*,†] Federica Zammillo,[a,†] Daniela Roldán,[a] Camilla Galletti,[a] Nunzio Russo[a], Simelys Hernández [a,b,*]

[a] *CREST group, Department of Applied Science and Technology (DISAT), Politecnico di Torino, C.so Duca degli Abruzzi, 24, 10129, Turin, Italy.*

[b] Center for Sustainable Future Technologies (IIT@PoliTo), *IIT – Istituto Italiano di Tecnologia, Via Livorno, 60, 10144, Turin, Italy.*

† These authors contributed equally to this work.

* *Corresponding author. E-mail address:* hilmar.guzman@polito.it, simelys.hernandez@polito.it

Supporting Information

Summary

S1. Electrochemical cell configurations

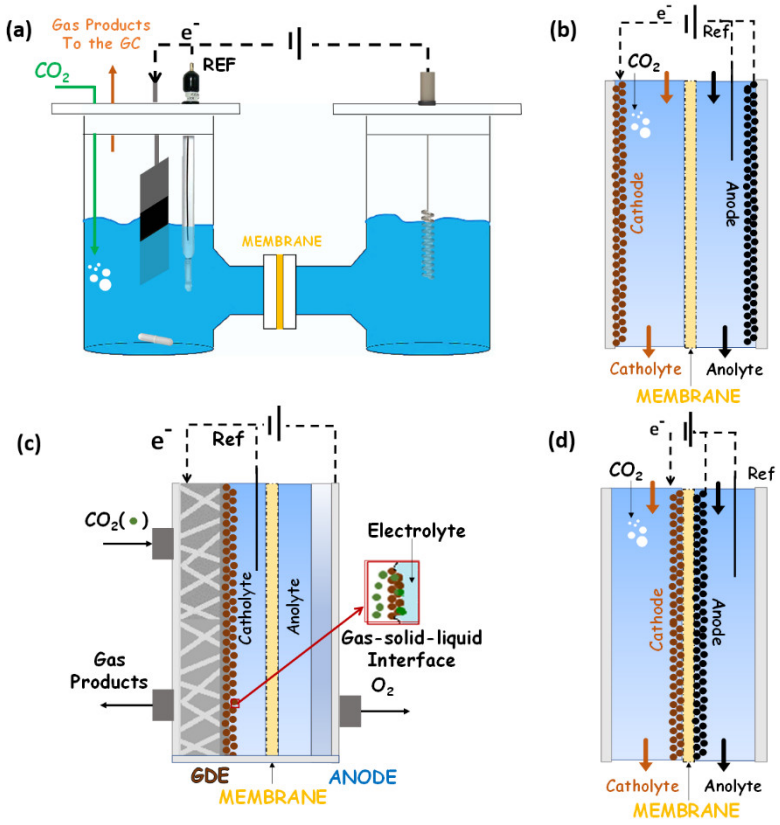

Figure S1. Schematic concepts of (a) H-type cell, (b) two compartments cell, (c) Gas Diffusion Electrode cell and (d) Membrane Electrode Assembly for electrochemical CO_2 reduction reactions.

S2. Standard reduction potentials for electrochemical CO_2 reduction

Table S1. CO_2 reduction products and corresponding standard reduction potential (E0) vs Normal Hydrogen Electrode (NHE) at pH = 0.

Cathodic half-cell reaction	E^0, V vs. NHE at pH=0 [§]
$4H^+ + 4e^- \rightarrow 2H_2$	0.000
$CO_2 + 2H^+ + 2e^- \rightarrow CO + H_2O$	-0.105
$CO_2 + 2H^+ + 2e^- \rightarrow HCOOH$	-0.169
$CO_2 + 4H^+ + 4e^- \rightarrow HCHO + H_2O$	-0.141
$CO_2 + 6H^+ + 6e^- \rightarrow CH_3OH + H_2O$	0.017
$CO_2 + 8H^+ + 8e^- \rightarrow CH_4 + 2H_2O$	0.169
$2CO_2 + 10H^+ + 10\ e^- \rightleftarrows CH_3CHO + 3H_2O$	0.050
$2CO_2 + 12H^+ + 12\ e^- \rightleftarrows C_2H_5OH + 3H_2O$	0.084
$2CO_2 + 12H^+ + 12e^- \rightarrow C_2H_4 + 4H_2O$	0.079
$2CO_2 + 14H^+ + 14e^- \rightarrow C_2H_6 + 4H_2O$	0.142
$3CO_2 + 16H^+ + 16\ e^- \rightleftarrows CH_3(CO)CH_3 + 5H_2O$	-0.140
$3CO_2 + 18H^+ + 18e^- \rightarrow C_3H_7OH + 5H_2O$	0.099
$CO_2 + e^- \rightarrow CO^{\cdot -}$	-1.486 *

[§]All of the EC CO_2R standard potentials (E^0) here reported were calculated via Gibbs free energy of reaction values taken from [1]. *The E^0 value for the of the formation of the $CO_2^{\cdot -}$ radical is the only exception, which was calculated from the Nernst equation with E^o(at pH=7) = -1.90 V vs. NHE, as reported in [2,3].

S3. Method of synthesis

The synthesis procedure was inspired in a previous work with some modifications.[4] A solution of hydrated metal nitrates (i.e. $Cu(NO_3)_2$, $Zn(NO_3)_2$ and $Al(NO_3)_3$) was used as precursor of the different catalysts.. The concentrations are specified in the manuscript in section 3.2. The synthesis started by pumping with a peristaltic pump 40 ml of the nitrates' solution into a beaker with 200 ml of ultra-pure distilled water (immersed in a hot silicone oil bath to keep the temperature at 70 °C). The metal amounts used in the case of CuZA-06-03-01 catalyst were 1.5 g of Cu (24 mmol), 0.78 g of Zn (12 mmol), and 0.11 g of Al (4 mmol). For the CuZ-06-03 and Cu-06 catalysts, the respective metal amount were kept constant. A solution of Na_2CO_3 1M was used as precipitating agent. During the precipitation process, the pH and temperature were controlled. A MC720 pH Controller was employed and allowed to set the desired pH value (pH=7 in this case) and, using a peristaltic pump, automatically sending the necessary amount of precipitating agent to the beaker to maintain the pH at the desired value. The temperature was monitored with a thermocouple.

S4. Physico-chemical characterization of the employed catalysts

In this work, the morphological characterisation of the materials and the relative elemental composition of the samples was obtained by operating a Field Emission Scanning Electron Microscopy (ZEISS MERLIN FE-SEM) technique, equipped with an Energy Dispersive X-ray Spectroscopy System (EDS) operated at 3kV. The sample preparation consisted in the dispersion of a small amount of catalyst particles in isopropanol through ultrasonic mixing for 30 min and then in placing a drop of the dispersion on an amorphous carbon-coated copper grid. Finally, before the analysis, the sample was dried at room temperature. On the other hand, the materials were characterized by means of N_2 adsorption to obtain the main textural parameters such as the specific surface area, total pore volume and the pore size distribution. The N_2 adsorption/desorption isotherms at 77 K were measured in a volumetric equipment TriStar II 3020 supplied by Micromeritics. Before starting the analysis, the samples were pre-treated at 200 °C, in order to clean the surface of absorbed molecules that may be contaminants, moisture, impurities, etc. The atomic ratio, BET surface area and total pore volume of the synthesised materials are shown in Table S2.

Table S2. Main textural parameters of the synthesized CuZnAl-oxide based catalysts.

Catalyst	EDS, atomic ratio	BET surface area, $m^2\ g^{-1}$	Total pore volume, $cm^3\ g^{-1}$
Cu-06	Cu/O 1:1	18.4	0.11
CuZ-06-03	Cu/Zn 60:40	55.16	0.23
CuZA-06-03-01	Cu/Zn/Al 60:30:10	101.65	0.37

The crystallinity of the materials was investigated by using a Panalytical X'Pert PRO diffractometer working in Bragg-Brentano configuration and equipped with Cu Kα radiation (λ =1.5418 Å) set at 40 kV and 40 mA. The X-Ray Diffraction (XRD) technique allowed to obtain information about the crystallite sizes and phase purity: the Scherrer formula $D = k\lambda / \beta \cos \theta$ was employed for calculating the crystallite size, where D is the average crystallite size (nm), λ is the wavelength of X-ray radiation (0.15418 nm), k is the shape factor (0.90) and β is the full-width half maximum, which was corrected for instrumental broadening; the powder catalysts were examined in the 2θ range of 20-80° with a scanning step of 0.013°. After tests electrodes were examined in the 2θ range of 20-150° with a scanning step of 0.020°. The XRD patterns of the employed powders can be seen in Figure S2.

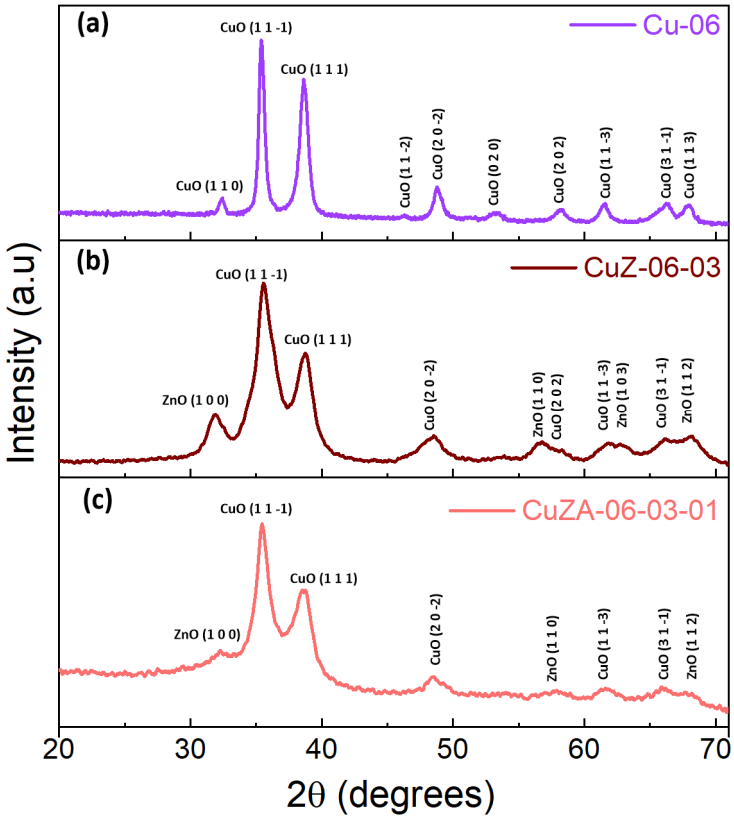

Figure S2. XRD patterns of CuZnAl-oxide based catalysts (a) Cu-06, (b) CuZ-06-03, (c) CuZA-06-03-01

Table S3. Crystallite sizes of the synthesized CuZnAl-oxide based catalysts.

Catalyst	Crystallite size, nm	
	from (11-1) reflection of CuO	from (100) reflection of ZnO
Cu-06	17	-
CuZ-06-03	7	7
CuZA-06-03-01	9	11

The presence of Cu, Zn and Al was further confirmed via inductively coupled plasma (ICP), with an iCAP 7600 DUO (Thermo Fisher Scientific). The chemical attack was carried out in a microwave oven. The treatment followed for the analysis was: i) ~ 100 mg of the sample was weighted; ii) it was solubilized in 10 ml of pure acid (6 mL HCl, 2 mL HNO_3 and 2 mL HF); iii) thermal treatment at 200 °C for 15 min with a ramp of 10°C min^{-1}; iv) cooling in about 30 min. The sample was then diluted to ~ 1 ppm with Milli-Q and filtered using a 0.45 µm PTFE filter before reading them with the instrument. The Cu/Zn/Al molar composition in the CuZA-06-03-01 catalyst is 52/39/9. Instead, the molar composition in the CuZ-06-03 catalyst is Cu/Zn = 56/44.

To investigate the chemical composition of their surface, XPS measurements were also performed on the Cu-06, CuZ-06-03 and CuZA-06-03-01 synthesised powders samples. The Cu2p doublet spectra in high resolution (not shown), display a common spectrum mainly related to CuO (Cu^{2+} satellite at 940-945 eV)[5]. The Cu^{2+} state has already been observed in bulk with XRD analysis. Since the deconvolution procedure of Cu2p spectra results complex due to the overlapping of binding energies of the different Cu oxidation states, Auger CuL3M4.5M4.5 region was also acquired with the aim of obtaining more details. The table in Figure S3 shows the modified Auger parameters of the samples with an average value (1851.8 ± 0.3 eV) that is typical of Cu^{2+} species, indicating that their surfaces are mainly composed of CuO (the sensible depth for XPS is 5 – 10 nm). Moreover, the amount of the Cu oxidation states and the ratio between Cu^{2+} and Cu^{0}+Cu^{1+}, were evaluated through the method developed by M. Biesinger and co-workers[5], by fitting the Cu2p3/2 peak and its related satellite. The results are reported in the Table in Figure S3, where it is possible to notice that the Cu-06 catalyst presents a higher percentage of Cu^{0}+Cu^{1+} (22%) than the CuZ-06-03 and CuZA-06-03-01 catalysts on the surface.

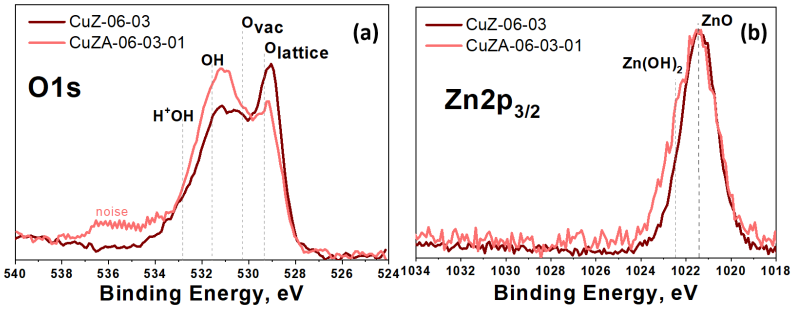

Catalyst	Auger Parameter, eV	Cu oxidation state	Cu^{2+}	Cu^{0} + Cu^{1+}
Cu-06	1851.6	Cu^{2+}	78%	22%
CuZ-06-03	1851.8	Cu^{2+}	92%	8%
CuZA-06-03-01	1852.1	Cu^{2+}	95%	5%

Figure S3. High resolution O1s (a) and Zn2p3/2 (b) XPS spectra of CuZ-06-03 and CuZA-06-03-01 catalysts and in the table the percentage of oxidation states of copper calculated from Auger parameter values on the surface of the CuZnAl-oxide based catalysts.

In addition, the high-resolution XPS spectra for O1s and Zn2p3/2 binding energy regions for the CuZ-06-03 and CuZA-06-03-01 catalysts are shown in Figure S3(a) and (b). The results revealed that the O species are divided into the following (Figure S3(a)): oxygen into the lattice structure (529.2 eV), oxygen vacancies (530.3 eV), and oxygen due to adsorbed molecules

(531.6 eV and 532.9 eV). These adsorbed molecules are related to weak basic sites on the surface: OH and H*OH, respectively, which mainly appear in the CuZA-06-03-01 powder material. Based on these results, it is possible to state that the conductivity of these metal oxides materials could be related to the presence of oxygen vacancies. Moreover, Zn is present as ZnO in both catalysts since the binding energy of the Zn2p3/2 peak is at around 1021.2 eV (see Figure S3(b)), while the peak at 1022.5 eV confirms the presence of $Zn(OH)_2$ species, which further indicates the alkalinity of the CuZA-06-03-01catalyst surface. As expected, the addition of ZnO and Al_2O_3, as amphoteric supports, enriched the surface basicity[6–8], which could enhance the catalytic activity and the adsorption of CO_2 molecule and *CO intermediate.

S5. Electrochemically Active Surface Area

The Electrochemically Active Surface Area (ECSA) values of the electrodes were calculated by determining the double-layer capacitances of a rough surface. The double-layer capacitances have been determined in a potential range where no Faradaic process occurs from CV measurements on N_2-purged electrolyte under rotation at 1300 rpm. This region is in a potential range with a 100 mV window potential centred at the open-circuit potential (OCP) of the system and, so, all the measured currents in this region were assumed to be from the double-layer charging. Then, the capacitive current density (i_c) was measured at different scan rates (5, 10, 25, 50, 75 and 100mV s^{-1}) from the recorded CV (see Figure S4). At the basis of this hypothesis, the i_c was equivalent to the product of electrochemical double layer capacitance, (C_{DL}) and the scan rate (v), as given in equation (S1).[9–11]

$$i_c = v.C_{DL} \quad \text{(S1)}$$

The C_{DL} is represented by the slope of the linear fitting when the i_c is plotted against the multiple scan rates and the ECSA is calculated according to the equation (S2), where C_{ref} is the double-layer capacitance of a flat reference surface. In this work was used a value of 28 μF cm^{-2} as a reference for a flat Cu electrode surface.[12,13]

$$ECSA = \frac{C_{DL}}{C_{ref}} \quad \text{(S2)}$$

The CuO catalyst could be reduced to Cu_2O and Cu at potentials even more positive than +0.2 V vs. RHE[14]. For this reason, in the applied potential range that was used for measuring the C_{DL} (from 0.0 to +1.2 V vs. RHE), most of the electrode is considered reduced. It can be assumed that the oxide-derived Cu metal is the contributor to evaluate the C_{DL} of the electrode. As shown in Table S4, the electrocatalysts exhibit drastically different surface areas. The highest ECSA of the mixed-metal oxide electrodes (CuZA and CuZ) is ascribed to their smaller crystallites with respect to the Cu-06 sample (see Table S3). However, adding Al_2O_3 was not so successful in increasing the ECSA as in the case of the only addition of ZnO to the Cu-based catalyst: in fact, Al_2O_3 was effective in increasing the BET surface area (see Table S2) but not the electrochemical active one.

Table S4. Capacitance and ECSA values of the electrodes.

Electrodes	C_{DL}, mF cm^{-2}	ECSA, cm^2
Cu foil	0.028	1
Cu-06	0.3	9.7
CuZ-06-03	3.5	123.9
CuZA-06-03-01	0.8	30.2

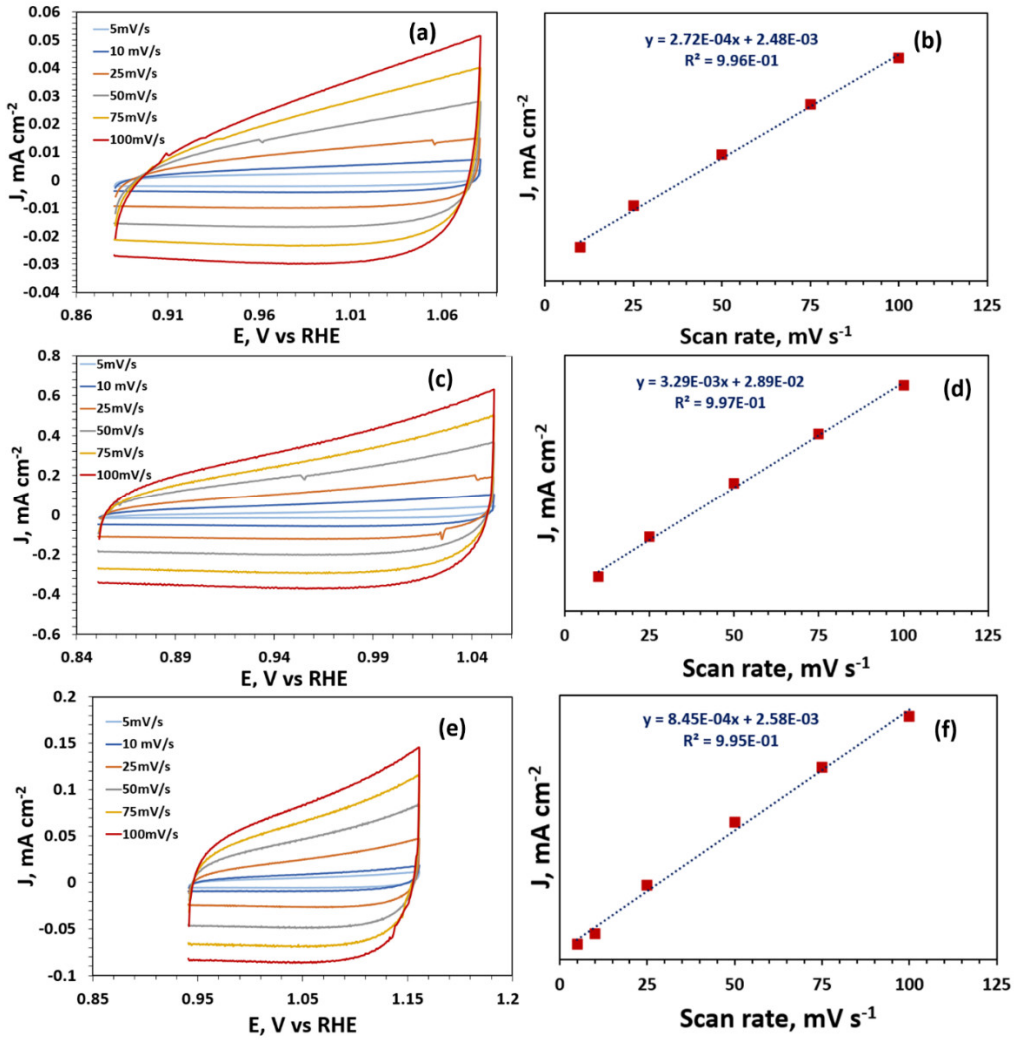

Figure S4. Determination of relative roughness (geometric area 0.0706 cm^2) of Cu-06 catalyst: a) Capacitive cycling of electrode over a 100 mV non-Faradaic region in a N_2-saturated 0.1 M $KHCO_3$ electrolyte, b) Capacitive current densities vs scan rate. CuZ-06-03 catalyst: c) Capacitive cycling of electrode over a 100 mV non-Faradaic region in a N_2-saturated 0.1 M $KHCO_3$ electrolyte, d) Capacitive current densities vs scan rate CuZ-06-03 catalyst: e) Capacitive cycling of electrode over a 100 mV non-Faradaic region in a N_2-saturated 0.1 M $KHCO_3$ electrolyte, f) Capacitive current densities vs scan rate. The measurements were carried in a RDE system with a catalyst loading of 0.6 mg_{CuO} cm^{-2}.

S6. Electroactivity in a Rotating Disk Electrode System

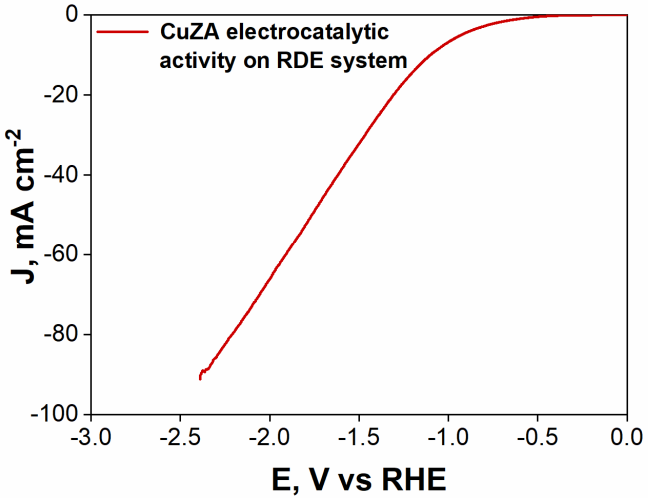

Figure S5. LSV responses under CO_2 flow of CuZA-06-03-01 catalysts in a Rotating Disk Electrode System. The test was carried out in CO_2-purged 0.1 M $KHCO_3$ electrolyte (scan rate: 5 mV s^{-1}) with a catalyst loading of 0.6 mg_{CuO} cm^{-2}.

S7. Blank test

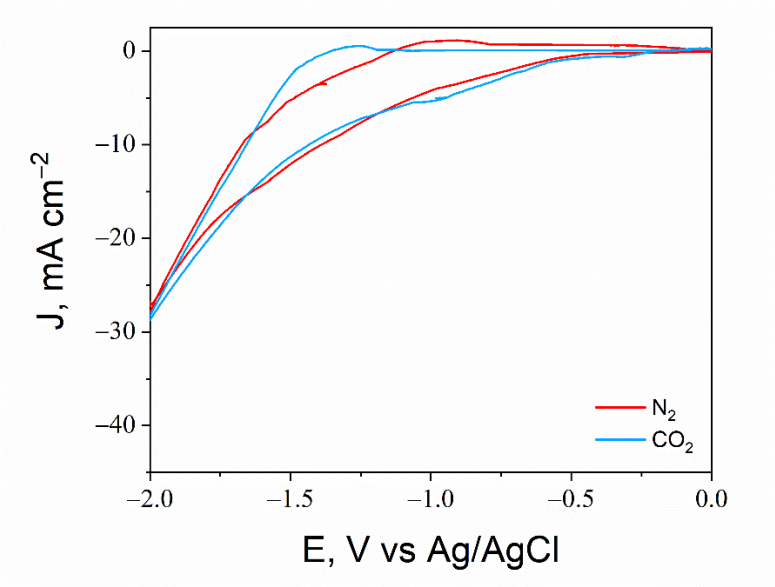

Figure S6. CV responses for a electrode with a ink without catalyst nanoparticles. The VC/Nafion ratio was 70/30, and the test was carried out in 0.1M $KHCO_3$ aqueous electrolyte.

From a blank test by using only Vulcan Carbon and Nafion in the GDE, contrary to what reported by Tung-Mo Tseng and co-workers,[15] within the potential range of 0 to -2.0 V vs Ag/AgCl, it was possible to clearly observe an increase in the activity towards hydrogen evolution both under N_2 and CO_2 flows (see Figure S6). The absence of redox peaks at -1.0 V vs Ag/AgCl in this blank test could confirm the hypothesis about the reduction of the Cu^{2+} species to Cu^{1+} and/or Cu^0 on the electrode containing the catalyst particles. The CV response under CO_2 flow is almost overlapped to that recorded under N_2. Therefore, from these observations, one might conclude that without the Cu-based catalyst particles almost only HER would be possible. However, it can be observed in Figure S7 that a very small amount of CO_2 reduction products (< 2%) was generated under chronoamperometry conditions.

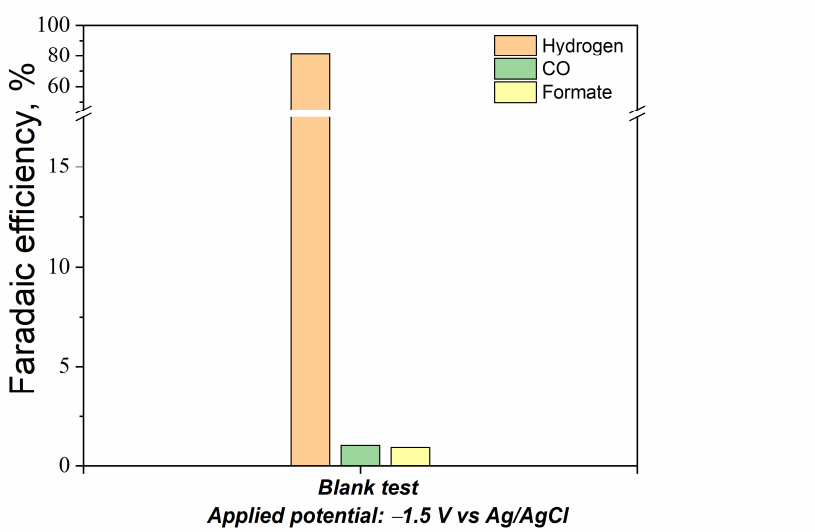

Figure S7. Faradaic efficiencies of gas and liquid products at -1.5 V vs Ag/AgCl for a electrode with a ink without catalyst nanoparticles. The chronoamperometry was carried out in 0.1M $KHCO_3$ aqueous electrolyte.

S8. Effect of local pH

Considering the control volume shown in the figure below (Figure S8), the boundary conditions that solution must meet are established. Particularly, in x = 0 µm (hence, at the GDL/electrolyte interface or left-hand boundary) the following conditions are enforced:

a) CO_2 concentration is set to its maximum solubility in a specified bulk electrolyte concentration;
b) No-flux condition is applied to OH^-, HCO_3^- and CO_3^{2-}.

In x = δ (corresponding to the diffusion layer thickness or right-hand boundary) the conditions are instead:

c) No-flux condition is applied to CO_2;
d) OH-, HCO_3^- and CO_3^{2-} concentrations are set to the equilibrium value in a specified bulk electrolyte concentration.

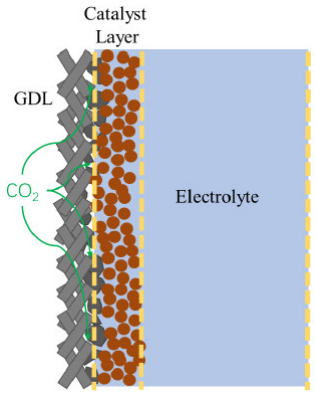

Figure S8. Schematic of the control volume. Adapted from Lv et al. [16]

The effective diffusion coefficient values were employed instead of the bulk values, as suggested in the work done by Raciti *et al.*[17], which identified the effective diffusivity to be in the range of 0.4-0.6D_b (being D_b the bulk diffusivity). The diffusion coefficient values and the kinetic constants are reported in the Table S5 and Table S6 below.

Table S5. Effective and bulk diffusion coefficients of chemical species in the bulk electrolyte at 25°C. [17]

Species	Effective diffusion coefficient D_{eff}, $m^2 s^{-1}$ [$D_{eff} = 0.6D_b$]	Bulk diffusion coefficient, $m^2 s^{-1}$
CO_2	$1.15 \cdot 10^{-9}$	$1.91 \cdot 10^{-9}$
HCO_3^-	$5.54 \cdot 10^{-10}$	$9.23 \cdot 10^{-10}$
CO_3^{2-}	$7.14 \cdot 10^{-10}$	$1.19 \cdot 10^{-9}$
OH^-	$3.16 \cdot 10^{-9}$	$5.27 \cdot 10^{-9}$

Table S6. Rate constants for forward and reverse reaction at 25°C.[18]

Reaction	Forward rate constant, 1 $M^{-1} s^{-1}$	Reverse rate constant, 1 s^{-1}
$CO_{2(aq)} + OH^- \overset{k1r\ k1f}{\Longleftrightarrow} HCO_3^-$	$k_{1f} = 5.93\ 10^3$	$k_{1r} = 1.34\ 10^{-4}$
$HCO_3^- + OH^- \overset{k2r\ k2f}{\Longleftrightarrow} CO_3^{2-} + H_2O$	$k_{2f} = 1\ 10^8$	$k_{2r} = 2.15 \cdot 10^4$

The equilibrium concentrations were determined on the basis of the equilibrium constants K_1 and K_2. The equilibrium constant K_1 can be derived as Eq. (S3):

$$K_1 = \frac{[HCO_3^-]}{[CO_2][OH^-]} \tag{S3}$$

Similarly, the equilibrium constant K_2 can be derived as Eq. (S4):

$$K_2 = \frac{[CO_3^{2-}]}{[HCO_3^-][OH^-]} \tag{S4}$$

The total concentration of dissolved carbonate forms (TC) is expressed as follows in Eq. (S5):

$$TC = [CO_2] + [HCO_3^-] + [CO_3^{2-}] \tag{S5}$$

Then, $[HCO_3^-]$ and $[CO_3^{2-}]$ can be derived from Eqs. (S3) - (S5) as follows:

$$[HCO_3^-] = \frac{K_1\,[OH^-]\,TC}{(1+K_1\,[OH^-]+K_1K_2[OH^-]^2)}$$

$$[CO_3^{2-}] = \frac{K_1K_2\,[OH^-]^2\,TC}{(1+K_1\,[OH^-]+K_1K_2[OH^-]^2)}$$

which depend on the TC and on the measured pH values.

The maximum solubility values were adopted from the reports by Gupta et al. and by Lv et al., with $[CO_2]$ = 34.2 mM in 0.1 M $KHCO_3$, $[CO_2]$ = 23.9 mM in 1 M $KHCO_3$, $[CO_2]$ = 27.7 mM in 1 M KCl, $[CO_2]$ = 24.5 mM in 1 M KOH and $[CO_2]$ = 25.7 mM in 0.5 M K_2SO_4.[16,18]

As the production of OH^- and the consumption of CO_2 occur within the catalyst layer, the terms of generation are spatially-dependent. Hence, they were evaluated as follows [19] in Eqs. (S6) and (S7):

$$R_{CO_2RR} = \frac{j}{F}\frac{\varepsilon}{L_{cat}}\frac{\sum_i FE_{i\,(CO_2RR)}}{n.e._i}\frac{[CO_2]}{[CO_{2,0}]} \qquad 0 \le x \le L_{cat} \tag{S6}$$

$$R_{CO_2RR} = 0 \qquad x > L_{cat}$$

$$R_{OH} = \frac{j}{F}\frac{\varepsilon}{L_{cat}}\left(1 - \frac{FE_{HCOO^-}}{n.e.}\right) \qquad 0 \le x \le L_{cat} \tag{S7}$$

$$R_{OH} = 0 \qquad x > L_{cat}$$

where j is the current density, F is the Faraday's constant, FE_i is the Faradaic efficiency of a given CO_2 reduction product, *n.e.* is the number of the electrons required for a given reduction reaction, L_{cat} is the width of catalyst layer and $\mathcal{E}$ is the porosity.

In literature, catalyst layer porosities in the range of 40-60% have been reported [20], thus it was assumed it to be 50%. The thickness of the catalyst layer should be determined via cross-sectional SEM. However, due to the lack of experimental data, it was supposed this value to be 2.5, 5, 10 or 20 μm depending on the catalyst loading. Specifically, the thickness values adopted were: 2.5 μm for the 0.44 mg/cm^2 GDE, 10 μm for the 2-2.5 mg/cm^2 GDE, 20 μm for the 4-4.5 mg/cm^2 GDE. The thickness of the diffusion layer was assumed to be 100μm, equal to that employed by Lv *et al.*[16] With this regard, an option would be to consider the diffusion

layer equal to the depth of the cavity into which the cathode is recessed due to the compression with a sealing gasket, as suggested by Dinh *et al.* [20]. Indeed, the fluid outside the cavity can be considered well mixed and continuously replaced.

In calculating Eqs. (S6) and (S7), the geometric current densities and product selectivities from these experimental results were imposed. Actually, in order to prove the validity of the model, it was attempted to reproduce the results obtained in the work done by Lv et al. The data obtained are in accordance with those reported in the literature.[16]

From the processing of our data, it was obtained the following trend in Figure S9 for the tests conducted on Cu-06 at -1.5, -1.75 and -2 V vs Ag/AgCl in 1M $KHCO_3$.

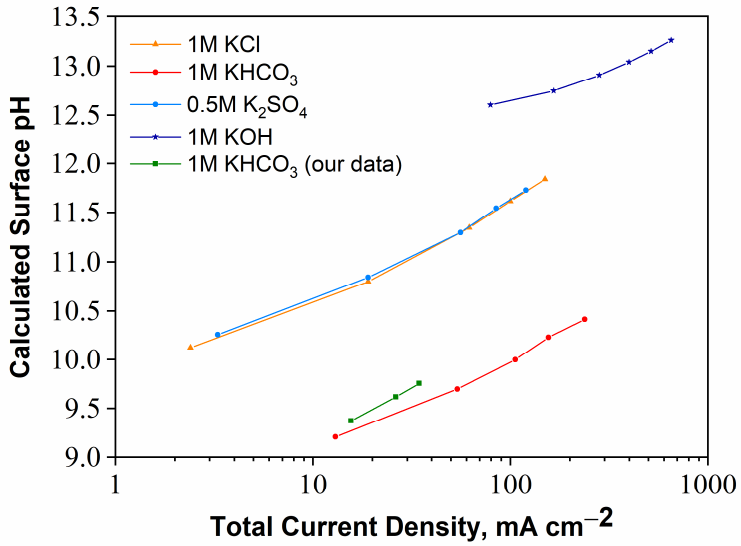

Figure S9. Surface pH trends obtained with the developed model: reproduction of the data reported by Lv et al. and processing of our experimental data (green curve) (obtained with tests conducted on Cu-06 catalyst at -1.5, -1.75 and -2 V vs Ag/AgCl in 1 M $KHCO_3$ electrolyte solution).

For a specific test, that is at -1.5 V vs Ag/AgCl, the impact of the supposed catalyst layer thickness was evaluated in order to set an error bar. As it can be seen in Figure S10, ranging from 2.5 µm to 20 µm resulted in a maximum variation of the calculated surface pH value equal to 0.05.

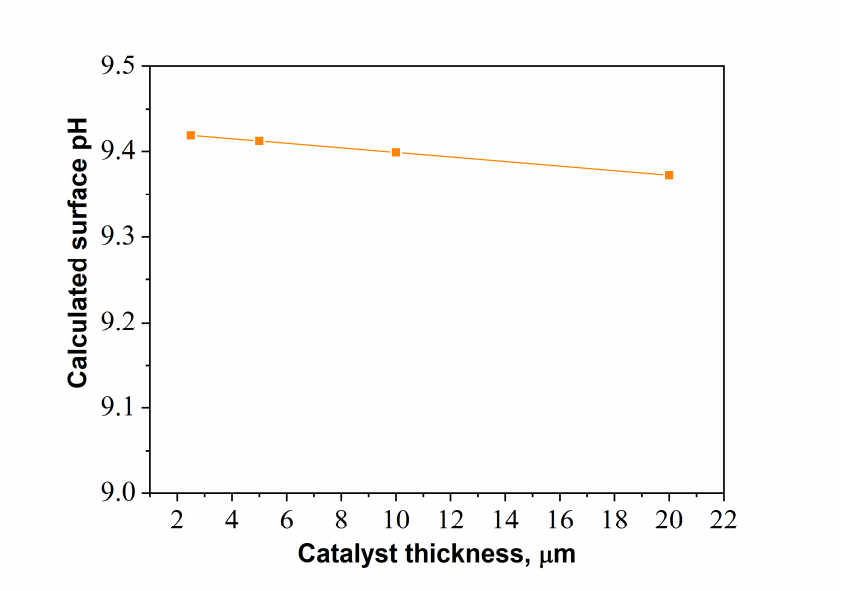

Figure S10. Influence of the catalyst thickness on the calculated surface pH for a specific test, conducted on Cu-06 catalysts at -1.5 V vs Ag/AgCl in 1 M $KHCO_3$ electrolyte solution.

S9. References

1. Ganesh, I. Electrochemical conversion of carbon dioxide into renewable fuel chemicals - The role of nanomaterials and the commercialization. *Renew. Sustain. Energy Rev.* **2016**, *59*, 1269–1297, doi:10.1016/j.rser.2016.01.026.
2. Richard Keene, F.; Creutz, C.; Sutin, N. Reduction of carbon dioxide by tris(2,2′-bipyridine)cobalt(I). *Coord. Chem. Rev.* **1985**, *64*, 247–260, doi:10.1016/0010-8545(85)80053-9.
3. Schwarz, H.A.; Dodson, R.W. Reduction potentials of CO_2^- and the alcohol radicals. *J. Phys. Chem.* **1989**, *93*, 409–414, doi:10.1021/j100338a079.
4. Baltes, C.; Vukojević, S.; Schüth, F. Correlations between synthesis, precursor, and catalyst structure and activity of a large set of $CuO/ZnO/Al_2O_3$ catalysts for methanol synthesis. *J. Catal.* **2008**, *258*, 334–344, doi:10.1016/j.jcat.2008.07.004.
5. Biesinger, M.C.; Lau, L.W.M.; Gerson, A.R.; Smart, R.S.C. Resolving surface chemical states in XPS analysis of first row transition metals, oxides and hydroxides: Sc, Ti, V, Cu and Zn. *Appl. Surf. Sci.* **2010**, *257*, 887–898, doi:10.1016/j.apsusc.2010.07.086.
6. Hall, A.S.; Yoon, Y.; Wuttig, A.; Surendranath, Y. Mesostructure-Induced Selectivity in CO_2 Reduction Catalysis. *J. Am. Chem. Soc.* **2015**, *137*, 14834–14837, doi:10.1021/jacs.5b08259.
7. Xiao, J.; Mao, D.; Guo, X.; Yu, J. Effect of TiO_2, ZrO_2, and TiO_2-ZrO_2 on the performance of CuO-ZnO catalyst for CO_2 hydrogenation to methanol. *Appl. Surf. Sci.* **2015**, *338*, 146–153, doi:10.1016/j.apsusc.2015.02.122.
8. Witoon, T.; Kachaban, N.; Donphai, W.; Kidkhunthod, P.; Faungnawakij, K.; Chareonpanich, M.; Limtrakul, J. Tuning of catalytic CO_2 hydrogenation by changing composition of CuO-ZnO-ZrO_2 catalysts. *Energy Convers. Manag.* **2016**, *118*, 21–31, doi:10.1016/j.enconman.2016.03.075.

9. Clark, E.L.; Resasco, J.; Landers, A.; Lin, J.; Chung, L.T.; Walton, A.; Hahn, C.; Jaramillo, T.F.; Bell, A.T. Standards and Protocols for Data Acquisition and Reporting for Studies of the Electrochemical Reduction of Carbon Dioxide. *ACS Catal.* **2018**, *8*, 6560–6570, doi:10.1021/acscatal.8b01340.

10. McCrory, C.C.L.; Jung, S.; Peters, J.C.; Jaramillo, T.F. Benchmarking heterogeneous electrocatalysts for the oxygen evolution reaction. *J. Am. Chem. Soc.* **2013**, *135*, 16977–16987, doi:10.1021/ja407115p.

11. McCrory, C.C.L.; Jung, S.; Ferrer, I.M.; Chatman, S.M.; Peters, J.C.; Jaramillo, T.F. Benchmarking Hydrogen Evolving Reaction and Oxygen Evolving Reaction Electrocatalysts for Solar Water Splitting Devices. *J. Am. Chem. Soc.* **2015**, *137*, 4347–4357, doi:10.1021/ja510442p.

12. Waszczuk, P.; Zelenay, P.; Sobkowski, J. Surface interaction of benzoic acid with a copper electrode. *Electrochim. Acta* **1995**, *40*, 1717–1721, doi:10.1016/0013-4686(95)00088-V.

13. Zeng, J.; Bejtka, K.; Ju, W.; Castellino, M.; Chiodoni, A.; Sacco, A.; Farkhondehfal, M.A.; Hernández, S.; Rentsch, D.; Battaglia, C.; et al. Advanced Cu-Sn foam for selectively converting CO_2 to CO in aqueous solution. *Appl. Catal. B Environ.* **2018**, *236*, 475–482, doi:10.1016/j.apcatb.2018.05.056.

14. Zeng, J.; Bejtka, K.; Di Martino, G.; Sacco, A.; Castellino, M.; Re Fiorentin, M.; Risplendi, F.; Farkhondehfal, M.A.; Hernández, S.; Cicero, G.; et al. Microwave-Assisted Synthesis of Copper-Based Electrocatalysts for Converting Carbon Dioxide to Tunable Syngas. *ChemElectroChem* **2020**, *7*, 229–238, doi:10.1002/celc.201901730.

15. Tseng, T.-M.; Huang, R.-H.; Huang, C.-Y.; Liu, C.-C.; Hsueh, K.-L.; Shieu, F.-S. Carbon Felt Coated with Titanium Dioxide/Carbon Black Composite as Negative Electrode for Vanadium Redox Flow Battery. *J. Electrochem. Soc.* **2014**, *161*, A1132–

A1138, doi:10.1149/2.102406jes.

16. Lv, J.J.; Jouny, M.; Luc, W.; Zhu, W.; Zhu, J.J.; Jiao, F. A Highly Porous Copper Electrocatalyst for Carbon Dioxide Reduction. *Adv. Mater.* **2018**, *30*, 1–8, doi:10.1002/adma.201803111.

17. Raciti, D.; Mao, M.; Wang, C. Mass transport modelling for the electroreduction of CO_2 on Cu nanowires. *Nanotechnology* **2018**, *29*, 10pp.

18. Gupta, N.; Gattrell, M.; MacDougall, B. Calculation for the cathode surface concentrations in the electrochemical reduction of CO_2 in $KHCO_3$ solutions. *J. Appl. Electrochem.* **2006**, *36*, 161–172, doi:10.1007/s10800-005-9058-y.

19. García de Arquer, F.P.; Dinh, C.T.; Ozden, A.; Wicks, J.; McCallum, C.; Kirmani, A.R.; Nam, D.H.; Gabardo, C.; Seifitokaldani, A.; Wang, X.; et al. CO_2 electrolysis to multicarbon products at activities greater than 1 A cm^{-2}. *Science (80-.).* **2020**, *367*, 661–666, doi:10.1126/science.aay4217.

20. Dinh, C.T.; Burdyny, T.; Kibria, G.; Seifitokaldani, A.; Gabardo, C.M.; Pelayo García De Arquer, F.; Kiani, A.; Edwards, J.P.; De Luna, P.; Bushuyev, O.S.; et al. CO_2 electroreduction to ethylene via hydroxide-mediated copper catalysis at an abrupt interface. *Science (80-.).* **2018**, *360*, 783–787, doi:10.1126/science.aas9100.